

Characterization of just one atom using synchrotron X-rays

<https://doi.org/10.1038/s41586-023-06011-w>

Received: 23 December 2020

Accepted: 24 March 2023

Published online: 31 May 2023

 Check for updates

Tolulope M. Ajayi^{1,2}, Nozomi Shirato¹, Tomas Rojas^{3,4}, Sarah Wieghold⁵, Xinyue Cheng⁶, Kyaw Zin Latt¹, Daniel J. Trainer¹, Naveen K. Dandu³, Yiming Li⁷, Sineth Premarathna^{1,2}, Sanjoy Sarkar², Daniel Rosenmann¹, Yuzi Liu¹, Nathalie Kyritsakas⁸, Shaoze Wang², Eric Masson⁶, Volker Rose⁵✉, Xiaopeng Li⁹, Anh T. Ngo^{3,4} & Saw-Wai Hla^{1,2}✉

Since the discovery of X-rays by Roentgen in 1895, its use has been ubiquitous, from medical and environmental applications to materials sciences^{1–5}. X-ray characterization requires a large number of atoms and reducing the material quantity is a long-standing goal. Here we show that X-rays can be used to characterize the elemental and chemical state of just one atom. Using a specialized tip as a detector, X-ray-excited currents generated from an iron and a terbium atom coordinated to organic ligands are detected. The fingerprints of a single atom, the L_{2,3} and M_{4,5} absorption edge signals for iron and terbium, respectively, are clearly observed in the X-ray absorption spectra. The chemical states of these atoms are characterized by means of near-edge X-ray absorption signals, in which X-ray-excited resonance tunnelling (X-ERT) is dominant for the iron atom. The X-ray signal can be sensed only when the tip is located directly above the atom in extreme proximity, which confirms atomically localized detection in the tunnelling regime. Our work connects synchrotron X-rays with a quantum tunnelling process and opens future X-rays experiments for simultaneous characterizations of elemental and chemical properties of materials at the ultimate single-atom limit.

X-ray characterization of materials has been revolutionized after the invention of synchrotron X-rays in the mid-twentieth century^{1–7}. The capabilities of synchrotron light sources have been continuously upgraded to improve resolution and minimum sample quantity required for measurements^{6–10}. So far, an attogram amount of sample can be detected by X-rays. However, it is still in the range of $\geq 10^4$ atoms and gaining access to a much smaller sample is becoming extremely arduous. If X-rays could be used to detect just one atom, it would further revolutionize their applications to an unprecedented level, from quantum information technology to environmental and medical research^{11–13}. One way to overcome these challenges is to supplant conventional detectors with a specialized detector made of a sharp metal tip positioned at extreme proximity to the sample to collect X-ray-excited electrons, a technique known as synchrotron X-ray scanning tunnelling microscopy (SX-STM)^{14,15–17} (Extended Data Fig. 1). X-ray spectroscopy in SX-STM is triggered by photoabsorption of core-level electrons, which constitutes elemental fingerprints (see Methods) and, thus, SX-STM is efficacious in identifying the elemental type of the materials directly. Moreover, instead of performing separate STM and X-ray experiments^{2,18,19}, SX-STM enables both measurements simultaneously at the same sample location^{17,20} and, thus, it is advantageous. There are two SX-STM measurement regimes: tunnelling and far field. In the tunnelling regime, the X-ray-excited tunnelling process is

dominant (Extended Data Fig. 1). Here the tip is positioned above the sample in tunnelling range (about 0.5 nm). In the far-field regime, the tip is positioned at a distance of about 5 nm from the sample, which is out of tunnelling range, and only X-ray-ejected electrons contribute to the measurements.

Experiments

Our experiment is conducted at the XTIP²¹ beamline at the Advanced Photon Source and the Center for Nanoscale Materials at Argonne National Laboratory. For the detection of a 3d transition metal, a ring-shaped supramolecular assembly formed by terpyridine (tpy) ligand subunits is chosen as an archetype (Fig. 1a). Each ring-like structure is composed of seven $\langle \text{tpy}-\text{metal}-\text{tpy} \rangle$ bridges, in which six ruthenium (Ru) (II) ions and one iron (Fe) (II) ion act as metal linkers (Fig. 1a,b). They appear in STM images as approximately 5-nm-diameter rings composed of seven protrusions, in which each protrusion corresponds to a $\langle \text{tpy}-\text{metal}-\text{tpy} \rangle$ bridge (Fig. 1c,d) and only one Fe ion is present in the entire ring. To further demonstrate X-ray detection of a different metal, we have chosen a terbium (Tb) complex, in which the Tb (III) ion is well protected by three brominated pyridine-2,6-dicarboxamide (pcam-Br) ligands (Fig. 1e) (Supplementary Information). Dimer molecules, $[\text{Tb}(\text{pcam})_3]_2$ (Fig. 1f), are then formed by on-surface synthesis,

¹Nanoscience and Technology Division, Argonne National Laboratory, Lemont, IL, USA. ²Nanoscale and Quantum Phenomena Institute, Physics & Astronomy Department, Ohio University, Athens, OH, USA. ³Materials Science Division, Argonne National Laboratory, Lemont, IL, USA. ⁴Department of Chemical Engineering, University of Illinois Chicago, Chicago, IL, USA. ⁵Advanced Photon Source, Argonne National Laboratory, Lemont, IL, USA. ⁶Department of Chemistry and Biochemistry, Ohio University, Athens, OH, USA. ⁷Department of Chemistry, University of South Florida, Tampa, FL, USA. ⁸Molecular Tectonics Laboratory, University of Strasbourg, UMR UDS-CNRS 7140, Institut le Bel, Strasbourg, France. ⁹College of Chemistry and Environmental Engineering, Shenzhen University, Shenzhen, China. ✉e-mail: vrose@anl.gov; hla@ohio.edu

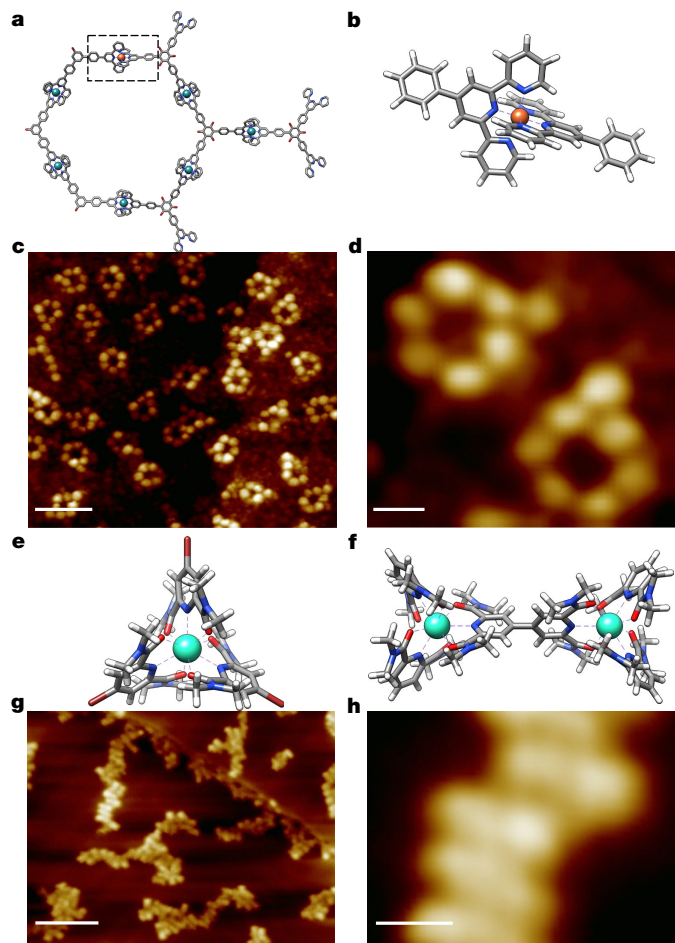


Fig. 1 | Structures of the metal–ligand complexes. **a**, Structure of the ring-shaped supramolecular assembly. Cyan = Ru, orange = Fe. **b**, The modelling structure of a *<tpy-Fe-tpy>* bridge shown by the dashed box in **a**. Orange = Fe atom, blue = N atoms. **c**, STM image showing the ring-shaped supramolecular assemblies. Scale bar, 10 nm. **d**, Zoomed-in area of the STM image depicts the detailed structure of two supramolecular assemblies. Scale bar, 2 nm. Image parameters for **c** and **d**: $I_t = 1.3 \times 10^{-11} \text{ A}$, $V_t = 2 \text{ V}$. **e**, Structure of $\text{Tb}(\text{pciam-Br})_3$. Cyan = Tb, brown = Br, red = O atoms. **f**, Structure of $[\text{Tb}(\text{pciam})_3]_2$. Red = O atoms, blue = N atoms. **g**, STM image showing clusters of $[\text{Tb}(\text{pciam})_3]_2$ on the surface. Scale bar, 8 nm. **h**, Zoomed-in area of the STM image showing individual dimer molecules in a cluster. Scale bar, 1 nm. Image parameters for **g** and **h**: $I_t = 3 \times 10^{-11} \text{ A}$, $V_t = 1 \text{ V}$.

in which two $\text{Tb}(\text{pciam})_3$ monomers are coupled through Ullmann-type dimerization²² on Au(111) (Fig. 1g,h and Extended Data Fig. 3).

In our SX-STM setup, both the sample and tip currents are simultaneously recorded (Fig. 2a). In the far-field regime (Fig. 2a), no electron tunnelling takes place and both the sample and tip currents are purely composed of the electrons ejected from the sample¹⁶. The X-ray absorption spectroscopy (STM-XAS) data in the far field show the L_{3} and L_{2} absorption edges of Fe ions in both the sample and tip currents at 708.9 eV and 722.1 eV produced by the $2p_{3/2}$ and $2p_{1/2}$ transitions of Fe to the unoccupied d orbitals, respectively (Fig. 2b,c). Although the entire illuminated sample area contributes to the background current, only the Fe ions generate the observed signals (Extended Data Fig. 4 and Supplementary Information). The photocurrent produced from the Fe ions, ΔI , is determined from the peak height relative to the base of the L_{3} edge (Fig. 2b). The sample current yields $\Delta I_{\text{Fe}}^s \approx 3.6 \text{ pA}$ (Fig. 2b), whereas the tip current gives $\Delta I_{\text{Fe}}^t \approx 0.03 \text{ pA}$ (Fig. 2c), which is about two orders of magnitude less than that of the sample. The sample current is generated by the entire X-ray-illuminated area, whereas the tip

captures <1% of the ejected electrons in the far field (Fig. 2b,c). Both the sample and tip currents here are contributed by the ensemble of identical Fe ions coordinated in several *<tpy-Fe-tpy>*. This experiment establishes the general detection of the Fe ion signal by the tip in the far field.

STM X-ray spectroscopy of one Fe atom

Next, the measurements are repeated in the tunnelling regime (Fig. 2d), in which the tip approaches the sample until a 100-pA tunnelling current is achieved at $\sim 1 \text{ V}$ bias. The experiment is performed by positioning the tip directly on top of or next to the supramolecular rings (Fig. 2e) and the results show two distinct sets of current profiles. The first set of spectra (Fig. 2f,g) is observed when the tip is not on the *<tpy-Fe-tpy>* bridge, such as position A in Fig. 2e, or on the *<tpy-Ru-tpy>* bridges (Extended Data Fig. 5). Here only the sample channel exhibits the $\text{FeL}_{2,3}$ edge signals with similar peak intensities as in the far field (Fig. 2f) because the sample current in the tunnelling regime is mainly contributed by the entire X-ray-illuminated area. However, the tip channel does not show any Fe edge signal (Fig. 2g) because the solid angle for photo-ejected electrons being captured by the tip is greatly reduced at very close tip–sample distance and the Fe edge signal from the entire X-ray-illuminated sample area is no longer detectable.

When the tip is positioned directly above the Fe atom in the *<tpy-Fe-tpy>* (position B in Fig. 2e), the second set of data (Fig. 2h,i) is observed. Remarkably, here the tip current not only shows cogent $\text{FeL}_{2,3}$ edges but also the current intensity, $\Delta I_{\text{Fe}}^t \approx 0.3 \text{ pA}$ (Fig. 2i), is an order of magnitude larger than the corresponding tip current of 0.03 pA in the far field (Fig. 2c). Thus, the X-ray-excited tunnelling process is dominant in the tunnelling regime in the tip channel (Fig. 2j). Because the quantum tunnelling process is extremely sensitive to the atomic positions²³, the Fe signal in the tip channel is observed only when the tip is located directly above the *<tpy-Fe-tpy>* in the tunnelling distance (Fig. 2i and Extended Data Fig. 6). Because only a single Fe ion is coordinated at the *<tpy-Fe-tpy>*, this signal is originated from just one Fe atom.

STM X-ray spectroscopy of one Tb atom

Next, we measured STM-XAS spectra on $\text{Tb}(\text{pciam-Br})_3$ complexes (Fig. 1e). Here cogent M_5 and M_4 adsorption edge signals of Tb produced by the $3d_{5/2}$ and $3d_{3/2}$ transitions of Tb to the unoccupied f orbitals are observed at 1,238.1 eV and 1,271.1 eV, respectively^{24–26}, both in the tunnelling (Fig. 3a,b and Supplementary Information) and far-field regimes (Extended Data Fig. 7). Like in the case of the Fe ion (Fig. 2f–i), the tip channel shows the Tb signal (Fig. 3b) only when the tip is located directly above the Tb ion in tunnelling distance (Extended Data Fig. 8). Then, to address the lateral-distance-dependent X-ray detection, we measure the M_5 edge signal of Tb in a $[\text{Tb}(\text{pciam})_3]_2$ dimer, in which two Tb ions are separated by about 1.24 nm by means of an organic linker (Fig. 1f–h, and Fig. 3c). Here a sequence of ten spectra (Fig. 3d and Supplementary Information) was acquired with a lateral distance of 0.18 nm between the spectra (Fig. 3c). Remarkably, only spectra 2 and 9 show cogent M_5 edge signals (Fig. 3d). Spectra 2 and 9 are roughly 1.26 nm apart, which agrees well with the distance between the two Tb ions. Thus, it unambiguously shows that the X-ray-excited current can be detected only when the tip is directly on top of the Tb ion in tunnelling distance but not on the ligands.

Next, the chemical states of single Fe and Tb ions are determined using the near-edge X-ray absorption fine structure (NEXAFS) method²⁷. The locations of the fine structures are specific to the types of ion, such as Tb(III) and Tb(IV), and Fe(II), Fe(III) and Fe(IV)^{25,26,28}. The STM-NEXAFS spectra measured at the M_5 edge of a single Tb ion in the tunnelling regime show six satellite peaks (Fig. 4a,b) at both the tip and sample channels. By averaging the tip and sample signals, they are found to be ‘i’ = 1,233.8 eV, ‘ii’ = 1,235.9 eV, ‘iii’ = 1,237.3 eV, ‘iv’ = 1,238.5 eV, ‘v’ = 1,240.5 eV and ‘vi’ = 1,242.6 eV, respectively. The spectra shapes here are akin to those

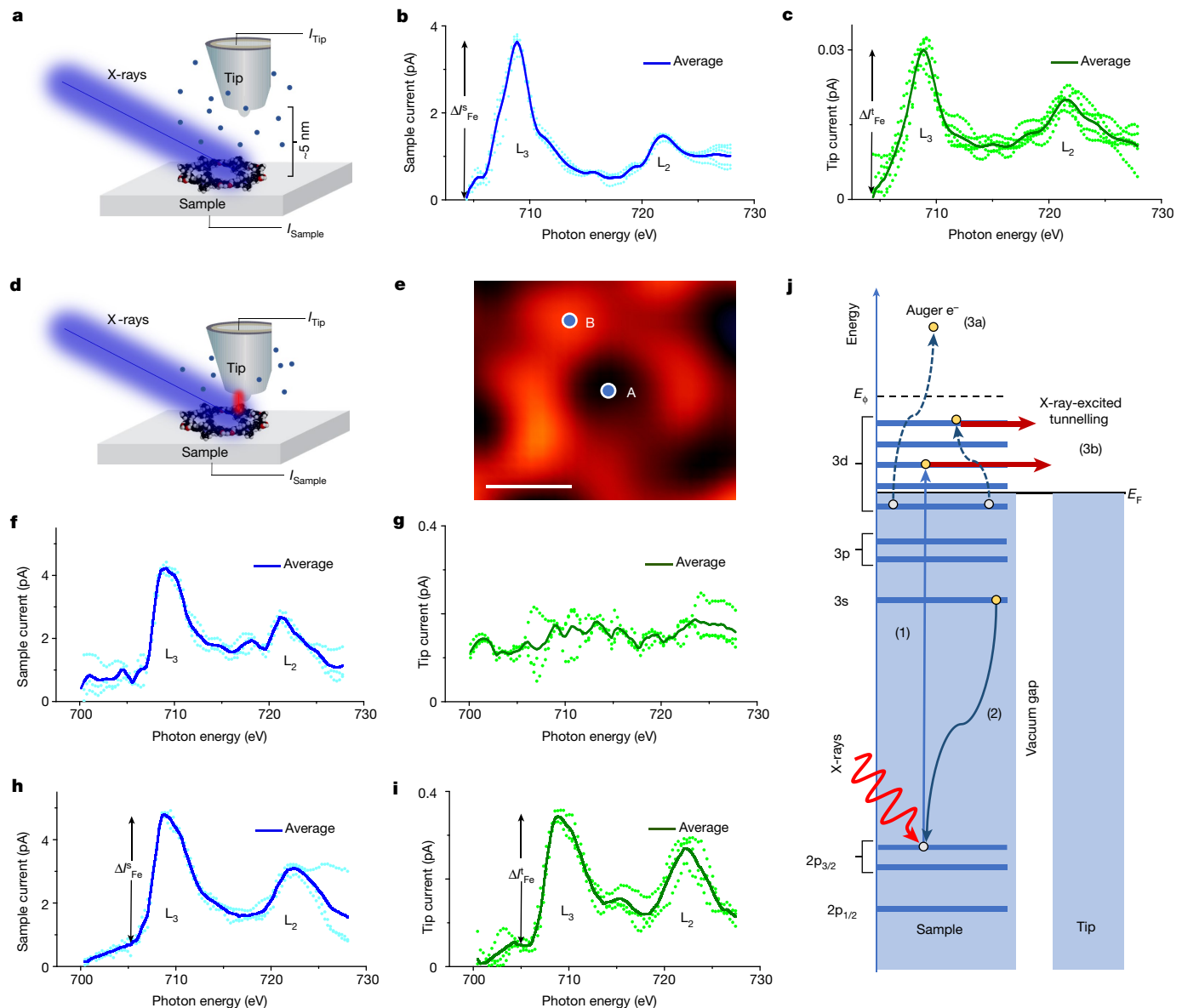


Fig. 2 | STM-XAS measurements of iron. **a**, Schematic of SX-STM in the far-field regime. **b**, STM-XAS spectra of the sample current. **c**, STM-XAS spectra of the tip current. **d**, Schematic of SX-STM in the tunnelling regime. **e**, STM image of a single supramolecular ring measured with the SX-STM setup. Image parameters: $I_t = 1 \times 10^{-11} \text{ A}$, $V_t = -1 \text{ V}$. Scale bar, 2 nm. **f–i**, Simultaneously recorded STM-XAS spectra of the sample and tip channels in the tunnelling regime when the tip is on position A (**f,g**) and when the tip is on position B (**h,i**).

j, X-ray-excited electron tunnelling process. Here (1) is the photoabsorption process, (2) depicts the filling of the vacancy by an electron from a higher orbit, (3a) is an example of an Auger process causing electron ejection and (3b) represents photoexcited tunnelling processes of primary and secondary electrons. In **b,c,f,g,h** and **i**, the initial current is set to zero and a linear slope is subtracted.

reported for Tb(III) ion in the literature measured over an ensemble average of the samples²⁶. Therefore, we can ascribe it as a Tb(III) ion.

Chemical states of Fe and Tb atoms

Next, to determine the chemical state of one Fe ion, STM-NEXAFS spectra are recorded at the L_3 edge region in the tunnelling regime (Fig. 4c,d). The sample channel shows six distinct fine structures. However, the shape and number of the satellite peaks in the tip channel seem to be markedly different where the peak ‘iv’ is missing. To check the result, we measure STM-NEXAFS spectra in the far field (Extended Data Fig. 9), in which the X-ray-excited tunnelling does not contribute to the spectra. Here six satellite peaks with similar energetic positions as the sample channel in the tunnelling regime (Fig. 4c) are observed in both the sample and tip channels, albeit the intensities of some peaks

are different. The positions of these satellite peaks are determined by averaging the tip and sample signals in the far field as ‘i’ = 707 eV, ‘ii’ = 708 eV, ‘iii’ = 708.7 eV, ‘iv’ = 709.3 eV, ‘v’ = 710.1 eV and ‘vi’ = 711.2 eV, respectively. From these data, we can ascribe it as a Fe(II) ion²⁸.

Unlike rare-earth elements such as Tb, the 3d electrons of Fe can strongly hybridize with the organic host. Therefore, the fine structures of Fe are not only specific to the ion type but also to their hybridizations with the ligands. To estimate the origin of the observed fine structures, unoccupied orbitals of a $\langle \text{tpy-Fe-tpy} \rangle$ adsorbed on a Au(111) surface are calculated using density functional theory (DFT). In $\langle \text{tpy-Fe-tpy} \rangle$ (Fig. 1b), the Fe ion hybridizes with the ligands through six nitrogen (N) atoms. In accord with the experiment, the projected density of states (PDOS) of the unoccupied Fe d and N p orbitals show six distinct states (Fig. 4e). Here the strong hybridization of Fe d_{xy} and d_{yz} orbitals with the N p_x and p_z orbitals forms the peak ‘i’, whereas its overlapping

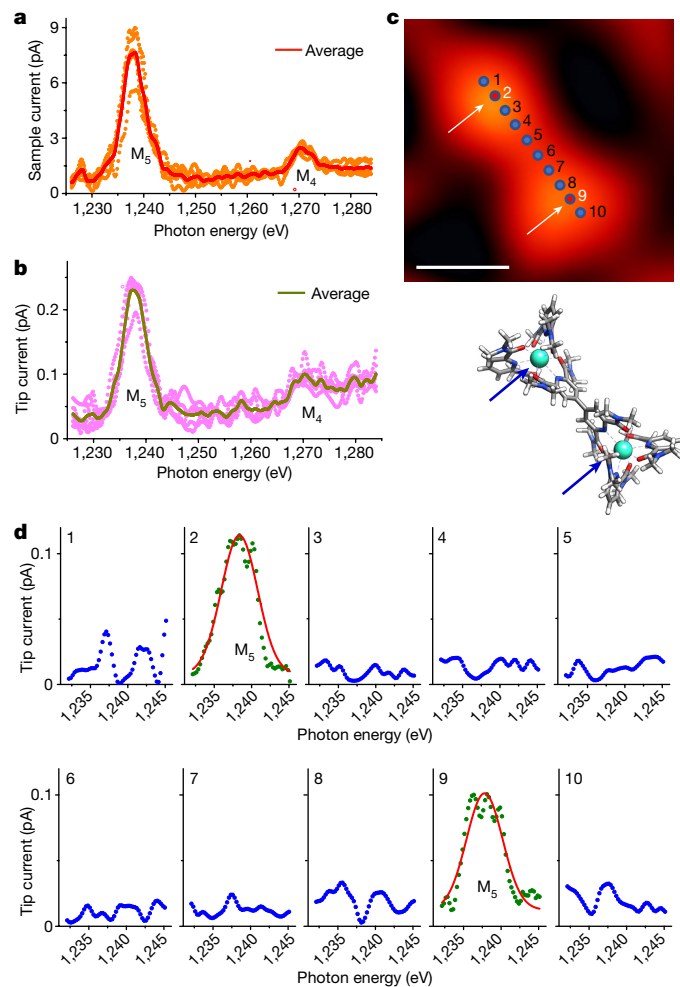


Fig. 3 | X-rays detection of Tb in the tunnelling regime. **a,b**, STM-XAS spectra of $M_{4,5}$ edges of Tb in the sample channel (**a**) and in the tip channel (**b**) measured in the tunnelling regime. **c**, STM image of a single $[Tb(\text{pcam})_3]_2$ complex measured with the SX-STM setup and a corresponding model. Image parameters: $I_t = 5 \times 10^{-11} \text{ A}$, $V_t = -1 \text{ V}$. The arrows in the STM image and the model indicate the two Tb ion locations. Scale bar, 1 nm. **d**, The sequence of STM-XAS spectra shows strong Tb M_5 peaks only at the two Tb ion locations, 2 and 9. The red lines in 2 and 9 are fits to the data. All the spectra in **d** are acquired with the same current setpoint. In **a**, **b** and **d**, the initial current is set to zero and a linear slope is subtracted.

satellite peak and the peak ‘ii’ are originated from the Fe d_{z^2} with N p_x and p_z hybridizations (Fig. 4e). The peak ‘iii’ corresponds to the Fe d_{x^2} orbital, whereas the peak ‘iv’ is from the hybridized Fe d_{z^2} and N p_y orbitals, respectively. Finally, the peaks ‘v’ and ‘vi’ are contributed from N p_x and p_z orbitals. The experimental and theoretical (Fig. 4e) energy separations of the peaks, ΔE , are in good agreement (Table 1).

Calculation also shows preferential adsorption of $\langle tpy\text{-Fe}\text{-tpy} \rangle$ on Au(111) with two tpy units forming as a cross (Fig. 4f). In such a geometry, the orbitals corresponding to the peaks ‘i’, ‘ii’, ‘iii’, ‘v’ and ‘vi’ have upward-pointing components, whereas that of the peak ‘iv’ is parallel to the surface (Fig. 4g). In the tunnelling regime, the tip current is mainly contributed by the tunnelling of X-ray-excited electrons that fill the unoccupied Fe d -N p hybridized orbitals (Fig. 2j). Both d and p orbitals are highly directional and a resonance tunnelling of overlapping d orbitals with the tip wavefunctions²⁹ can lead to preferential tunnelling of the upward-pointing orbitals to the tip (Fig. 4h). This process, which we named X-ERT (for X-ray-excited resonance tunnelling), occurs for all the orbitals except that of the peak ‘iv’. In the peak ‘iv’, the absence of upward orbital components inhibits the X-ERT process (Fig. 4i) and, hence, it is missing in the tip channel (Fig. 4d). By contrast, the sample

Table 1 | Comparison of ΔE between experiment and theory

	Experiment (eV)	Theory (eV)
$\Delta E_{i\text{-}ii}$	1.0	0.9
$\Delta E_{ii\text{-}iii}$	0.7	0.7
$\Delta E_{iii\text{-}iv}$	0.6	0.4
$\Delta E_{iv\text{-}v}$	0.8	0.9
$\Delta E_{v\text{-}vi}$	1.1	1.5

The energy difference between the satellite peaks observed in the experiment (Extended Data Fig. 9) and theory (Fig. 4e).

current is composed of both the X-ray-ejected electrons from the entire illuminated sample area as well as the X-ray-excited tunnelling at the tip location. Therefore, the STM-NEXAFS signal at the sample channel contains all peaks.

Conclusions

The following conclusions can be drawn from the above experiments: (1) the Fe signal can be detected in STM-XAS spectra on different parts of $\langle tpy\text{-Fe}\text{-tpy} \rangle$ (Extended Data Fig. 6), whereas the Tb signal is atomically localized (Fig. 3d); (2) in the STM-NEXAFS data, the spectra shapes and the missing satellite peak of the Fe ion (Fig. 4c,d) can be explained by the X-ERT process, whereas the Tb ion reproduces similar features between the tip and sample channels (Fig. 4a,b). Rare-earth metals have tantalizing electronic and magnetic properties for high-technological applications owing to their well-shielded 4f electrons³⁰. This is clearly observed in our one-atom measurements, in which the 4f orbitals of the Tb ion are isolated and are not involved in chemical bonding with the ligands, whereas the 3d orbitals of the Fe ion are heavily hybridized with its surroundings.

Online content

Any methods, additional references, Nature Portfolio reporting summaries, source data, extended data, supplementary information, acknowledgements, peer review information; details of author contributions and competing interests; and statements of data and code availability are available at <https://doi.org/10.1038/s41586-023-06011-w>.

- Wu, C.-Y. et al. High-spatial-resolution mapping of catalytic reactions on single particles. *Nature* **541**, 511–515 (2017).
- Rau, I. G. et al. Reaching the magnetic anisotropy limit of a 3d metal atom. *Science* **344**, 988–992 (2014).
- Lombi, E. & Susini, J. Synchrotron-based techniques for plant and soil science: opportunities, challenges and future perspectives. *Plant Soil* **320**, 1–35 (2009).
- van den Bedem, H. & Fraser, J. S. Integrative, dynamic structural biology at atomic resolution—it’s about time. *Nat. Methods* **12**, 307–318 (2015).
- Yano, J. & Yachandra, V. K. X-ray absorption spectroscopy. *Photosynth. Res.* **102**, 241–254 (2009).
- Bilderback, D. H., Elleaume, P. & Weckert, E. Review of third and next generation synchrotron light sources. *J. Phys. B At. Mol. Opt. Phys.* **38**, S773–S797 (2005).
- Eberhardt, W. Synchrotron radiation: a continuing revolution in X-ray science—diffraction limited storage rings and beyond. *J. Electron Spectrosc. Relat. Phenom.* **200**, 31–39 (2015).
- Chao, W. et al. Soft X-ray microscopy at a spatial resolution better than 15 nm. *Nature* **435**, 1210–1213 (2005).
- Meirer, F. et al. Synchrotron radiation-induced total reflection X-ray fluorescence analysis. *Trends Anal. Chem.* **29**, 479–496 (2010).
- Kotani, Y. et al. X-ray nanospectroscopy for attogram-scale two-dimensional nanomaterials using photoelectron emission microscopy. *AIP Conf. Proc.* **1234**, 437–440 (2010).
- Ívády, V. et al. Stabilization of point-defect spin qubits by quantum wells. *Nat. Commun.* **10**, 5607 (2019).
- Tagliabue, A. et al. The integral role of iron in ocean biogeochemistry. *Nature* **543**, 51–59 (2017).
- Gupta, V. B. et al. Aluminium in Alzheimer’s disease: are we still at a crossroad? *Cell. Mol. Life Sci.* **62**, 143–158 (2005).
- Saito, A. et al. Development of a scanning tunneling microscope for *in situ* experiments with a synchrotron radiation hard-X-ray microbeam. *J. Synchrotron Rad.* **13**, 216–220 (2006).
- Okuda, T. et al. Nanoscale chemical imaging by scanning tunneling microscopy assisted by synchrotron radiation. *Phys. Rev. Lett.* **102**, 105503 (2009).
- Rose, V. et al. Synchrotron X-ray scanning tunneling microscopy: fingerprinting near to far field transitions on Cu(111) induced by synchrotron radiation. *Adv. Funct. Mater.* **23**, 2646–2652 (2013).

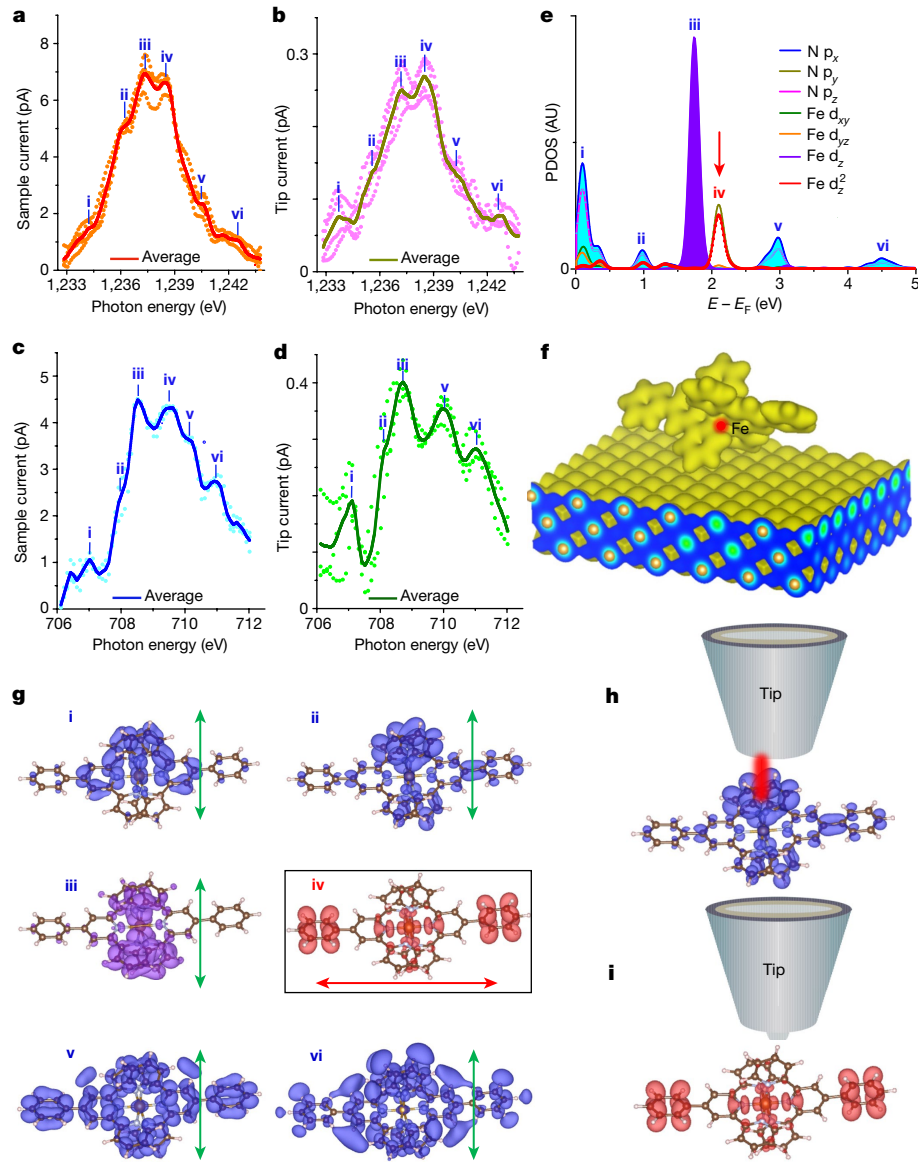


Fig. 4 | Single-atom chemical states and X-ERT. **a–d**, STM-NEXAFS signal of Tb ion measured at the sample channel (**a**) and at the tip channel (**b**) in the tunnelling regime. STM-NEXAFS signal of Fe ion measured at the sample channel (**c**) and at the tip channel (**d**) in the tunnelling regime. **e**, Calculated unoccupied PDOS of Fe and N atoms of <tpy-Fe-tpy>. Here ‘0’ is the Fermi level of the Au(111) substrate. **f**, Calculated 3D charge density plot of a <tpy-Fe-tpy> bridge on Au(111). The red arrow indicates the missing orbital in **d**.

g, Hybridized orbitals, in which ‘i’ to ‘vi’ correspond to the peaks shown in **e**. Here the green arrows indicate the orbitals having a surface-normal component, whereas the red arrow in ‘iv’ indicates the orbital having a surface-parallel component. **h**, X-ERT occurs when the orbital has a surface-normal component. **i**, The orbital ‘iv’ is located along the surface-parallel direction and X-ERT is not observed. AU, arbitrary units.

17. Shirato, N. et al. Elemental fingerprinting of materials with sensitivity at the atomic limit. *Nano Lett.* **14**, 6499–6504 (2014).
18. Mairena, A. et al. Stereospecific autocatalytic surface explosion chemistry of polycyclic aromatic hydrocarbons. *J. Am. Chem. Soc.* **140**, 7705–7709 (2018).
19. Wackerlin, C. et al. On-surface coordination chemistry of planar molecular spin systems: novel magnetochemical effects induced by axial ligands. *Chem. Sci.* **3**, 3154–3160 (2012).
20. Kersell, H. et al. Detecting element specific electrons from a single cobalt nanocluster with synchrotron X-ray scanning tunneling microscopy. *Appl. Phys. Lett.* **111**, 103102 (2017).
21. Rose, V. et al. XTIP – the world’s first beamline dedicated to the synchrotron X-ray scanning tunneling microscopy technique. *J. Synchrotron Rad.* **27**, 836–843 (2020).
22. Hla, S.-W., Bartels, L., Meyer, G. & Rieder, K.-H. Inducing all steps of a chemical reaction with the scanning tunneling microscope tip: towards single molecule engineering. *Phys. Rev. Lett.* **85**, 2777–2780 (2000).
23. Repp, J., Meyer, G., Olsson, F. E. & Persson, M. Controlling the charge state of individual gold adatoms. *Science* **305**, 493–495 (2004).
24. Margheriti, L. et al. X-ray detected magnetic hysteresis of thermally evaporated terbium double-decker oriented film. *Adv. Mater.* **22**, 5488–5493 (2010).
25. van der Laan, G., Fuggle, J. C., van Dijk, M. P. & Burggraaf, A. J. Determination of the relative concentrations of rare earth ions by X-ray absorption spectroscopy: application to terbium mixed oxides. *J. Phys. Chem. Solids* **47**, 413–416 (1986).
26. Thole, B. T. et al. 3d x-ray-absorption lines and the 3d⁹4fⁿ⁺¹ multiplets of the lanthanides. *Phys. Rev. B* **32**, 5107–5118 (1985).
27. Chang, H. et al. X-ray magnetic circular dichroism and near-edge X-ray absorption fine structure of buried interfacial magnetism measured by using a scanning tunneling microscope tip. *Appl. Phys. Lett.* **113**, 061602 (2018).
28. Ikeno, H. et al. First principles calculation of Fe $L_{2,3}$ -edge X-ray absorption near edge structures of iron oxides. *Mater. Trans.* **45**, 1414–1418 (2004).
29. Hla, S. W., Marinovic, V., Prodan, A. & Musevic, I. STM/AFM investigations of β -MoTe₂, α -MoTe₂ and WTe₂. *Surf. Sci.* **352–354**, 105–111 (1996).
30. Vincent, R., Klyatskaya, S., Ruben, M., Wernsdorfer, W. & Balestro, F. Electronic read-out of a single nuclear spin using a molecular spin transistor. *Nature* **488**, 357–360 (2012).

Publisher’s note Springer Nature remains neutral with regard to jurisdictional claims in published maps and institutional affiliations.

Springer Nature or its licensor (e.g. a society or other partner) holds exclusive rights to this article under a publishing agreement with the author(s) or other rightsholder(s); author self-archiving of the accepted manuscript version of this article is solely governed by the terms of such publishing agreement and applicable law.

© UChicago Argonne, LLC, Operator of Argonne National Laboratory, under exclusive licence to Springer Nature Limited 2023

Methods

Sample preparation

Fe-ion-containing complexes. The supramolecular assembly was synthesized through stepwise coordination and Suzuki coupling reactions³¹. This system has several advantages: (1) one assembly occupies a large surface area of about 25 nm², in which just one Fe ion is present; (2) the tpy bridge protects the Fe ion from the environment, preserving its electronic structure and chemical state. Structural analysis and calibration of deposition parameters for the supramolecular assemblies were performed on Au(111) and Ag(111) surfaces using a low temperature STM setup, whereas all the SX-STM measurements were performed on a Au(111) surface. The single-crystal surfaces were cleaned by repeated cycles of Ar ion sputtering and annealing up to 700 K under ultrahigh vacuum (UHV). A low sub-monolayer coverage of the supramolecular assemblies dissolved in a MeCN solution was drop cast onto the sample surface^{31,32} and then it was heated to about 400 K under UHV to remove some solvent molecules from the surface. Next, STM images were acquired at different locations of the sample to confirm successful deposition. After establishing proper deposition, the sample was transferred to the SX-STM end station at the XTIP beamline by means of a UHV suitcase (pressure $<2 \times 10^{-9}$ torr). The sample was imaged with SX-STM in STM mode to confirm its condition before the X-ray experiments.

Tb-ion-containing complexes. A sub-monolayer coverage of Tb(pcam-Br)₃ complexes (see Supplementary Information for synthesis and characterizations) was drop cast onto 200-nm-thick gold film formed on a mica substrate and annealed at 423 K for 30 min to remove residual solvent. The Tb M_{4,5} edge and NEXAFS measurements were performed on the sample. For the formation of Tb dimers, Tb(pcam-Br)₃ complexes were thermally deposited onto atomically clean Au(111) substrate under UHV. STM images were acquired to check the structure of the Tb(pcam-Br)₃ complexes adsorbed on Au(111) surface at 5 K (Extended Data Fig. 3). To form [Tb(pcam)₃]₂ dimers, the sample was heated to 473 K for 30 min. The formation of [Tb(pcam)₃]₂ was preceded by debromination and covalent linking of the two Tb(pcam)₃ complexes. There are three Br atoms at the initial molecules and, therefore, three bonds should be available for covalent linking. The formation of dimer molecules, [Tb(pcam)₃]₂, requires only one bond. We assume that the other two bonds are terminated by H atoms available on the surface inside the UHV system, as in the case of graphene nanoribbon formation on Au(111)³³. On covalent linking, the two Tb(pcam) units are slightly rotated from its initial plane to accommodate torsion along the biaryl axis. However, the Tb ion environment inside the ligand is the same as the monomers but the dimer includes a pair of Tb(III) ions separated by an organic linker (Fig. 1f). The dimers are not mobile during the scanning with the STM tip and their length fits with the expected length of the dimers linked by covalent bonding without Br atoms (Extended Data Fig. 3).

SX-STM mechanistic model

SX-STM XAS is performed by ramping the photon energy of a monochromatic X-ray beam illuminating the sample. When a photon is absorbed by a core electron, it is excited into unoccupied atomic/molecular orbitals above the Fermi level matching the energy difference ΔE . Further increasing the X-ray-beam energy can excite core electrons to higher unoccupied orbitals and, ultimately, to the continuum. The photoabsorption leads to excitation of the core electron leaving a core vacancy, which is subsequently filled by an electron from a higher-level orbit (Fig. 2j and Extended Data Fig. 1). The excess energy in this process produces Auger electrons. The lower-energy Auger electrons can fill up the unoccupied states between the Fermi level and the work function, and subsequently tunnel into the tip, contributing to the X-ray-excited tunnelling current. Some higher-energy

Auger electrons may be ejected, contributing to the X-ray-ejected current.

SX-STM measurements

STM-XAS and STM-NEXAFS measurements were performed at the XTIP²¹, the world's first user-dedicated beamline for SX-STM, at the sector 4-ID-E of the Advanced Photon Source and Center for Nanoscale Materials at Argonne National Laboratory. Using a spherical grating monochromator, the beamline can generate monochromatic X-rays with photon energies between 400 eV and 1,900 eV. After passing a zero-order slit, the beam is focused onto a movable exit slit (Extended Data Fig. 1). With the aid of the vertical and horizontal focusing mirrors, a final monochromatic X-ray beam of about 10 μm × 10 μm is incident onto the tip–sample junction of the SX-STM with an angle between 20° and 30° with respect to the sample surface plane. To properly illuminate the tip–sample junction, a beam alignment is performed by driving the microscope mounted on a motorized stage with four degrees of freedom relative to the beam and by adjusting the beam location vertically and horizontally with the Kirkpatrick–Baez focusing mirror pair. The X-ray beam is chopped into ON and OFF cycles using an X-ray chopper. During the OFF cycle, only the conventional tunnelling current is measured, which is used as the STM feedback signal to maintain the tip height in the tunnelling regime. During the ON cycle, the conventional tunnelling current is separated completely from the X-ray-excited current using a field-programmable gate array. Both sample and tip currents are simultaneously recorded by using separate lock-in amplifiers, which is greatly advantageous by allowing to systematically compare the tip and sample spectra. All the experiments are performed in UHV at approximately 30 K substrate temperature. Initially, the X-ray beam energy is calibrated by measuring Mn and Fe thin foil standards. Then, the SX-STM is first operated in the STM mode by closing the X-ray shutter to acquire topographic images using -1 V bias for the supramolecular assemblies and -0.5 V to -1.2 V for the Tb complexes. For the measurements in the tunnelling regime, the tunnelling current was set to 100 pA. After obtaining the STM images of the sample area, the X-ray shutter is opened and the tip–sample junction is illuminated with X-rays for the measurements. For the far-field STM-XAS experiments, the tip is retracted about 5 nm from the sample and remained static throughout the measurement. To detect the STM-XAS measurements, the X-ray-beam energy is ramped at the Fe L_{2,3} and Tb M_{4,5} absorption edge energy ranges (about 700 eV to 730 eV and 1,225 eV to 1,286 eV, respectively) using energy steps between 0.1 eV and 0.5 eV. In the supramolecular assembly, the Ru ions cannot be detected because the L₃ and L₂ absorption edges of Ru, 2,837.9 eV and 2,966.9 eV, respectively, are out of the photon energy range of the XTIP beamline²¹. For the lateral-distance-dependent X-ray detection on Tb-dimer molecules, the spectra were acquired with 0.25-eV energy steps. The resolving power of the monochromator was about 2,800 for the Fe and 1,400 for the Tb scans, respectively. At each energy step, an average signal is recorded from 50 data points for Fe and 40 data points for Tb.

With the photon flux of $2.5 \times 10^{11} \text{ s}^{-1}$ for the 10 μm × 10 μm X-ray beam at 709 eV (Extended Data Fig. 1d) and considering the incident X-ray beam angle of about 25° with respect to the sample surface, the photon flux density is estimated as $1.05 \times 10^{21} \text{ photons s}^{-1} \text{ m}^{-2}$. This corresponds to roughly 19.59 photons s⁻¹ hitting the Fe(II) ion ($r = 77 \text{ pm}$). Considering that 50% of the X-ray beam is blocked because of the X-ray ON–OFF cycles of the chopper, the number of X-ray photons hitting the Fe(II) ion is estimated as approximately 9.78 photons s⁻¹. Using the tip photocurrent of Fe L₃ absorption edge, 0.3 pA (Fig. 2i), the total X-ray-excited tunnelling electron yield of a single Fe(II) ion is determined as $1.86 \pm 0.07 \times 10^5$ electrons per photon. For the Tb(III) ion, the photon flux of $2 \times 10^{10} \text{ s}^{-1}$ for the 10 μm × 10 μm X-ray beam at about 1,240 eV with approximately 25° incident angle, the photon flux density is estimated as $8.45 \times 10^{19} \text{ photons s}^{-1} \text{ m}^{-2}$. This corresponds to about 19.3 photons s⁻¹ hitting the Tb(III) ion ($r = 118 \text{ pm}$). Considering

the X-ray ON–OFF cycle of the SX-STM, the number of X-ray photons hitting the Tb(III) ion is estimated to be about 9.66 photons s⁻¹. Using the tip photocurrent of Tb M₅ absorption edge, 0.22 pA (Fig. 3b), the total X-ray-excited tunnelling electron yield of a single Tb(III) ion is determined as $1.61 \pm 0.47 \times 10^5$ electrons per photon. The errors in X-ray-excited tunnelling electron yields for both Fe and Tb are generated from the statistical distributions. It should be noted that the X-ray excited tunnelling electron yields obtained by this simplified estimation seem to be rather large. Hence, the actual excitation process might be more complex than proposed here and requires further investigation.

Detector tips

The detector tips^{34,35} used for SX-STM are coaxial tips with a PtIr wire at the core acting as a conducting part, which collects electrons (Extended Data Fig. 2). This PtIr core is then coated with a SiO₂ insulating layer. Although the SiO₂ layer is insulating, photoelectron bombardment could result in capacitance charging, which—in turn—produces undesired noise in the recorded tip current. To prevent this, the tip is coated with a Au film on top of a thin titanium buffer³⁴. This outer Au layer can be grounded or can be supplied with a desired biasing voltage³⁵. In this work, the outer Au layer is grounded. To prepare a detector tip, first Pt₉₀Ir₁₀ tips are produced by etching a 250-μm-diameter wire in a 1.5-M calcium chloride solution. After selecting a sharp tip by electron microscope imaging, it is coated with an approximately 1-μm-thick SiO₂ layer, followed by a thin Ti buffer layer and, finally, an approximately 1-μm-thick Au outer layer. After coaxial film formation, focussed ion beam milling (shadow masking method) with a Zeiss 1540XB FIB-SEM (Ga⁺ ions, 50 kV, 50 pA) is performed at the nanofabrication facility of the Center for Nanoscale Materials to expose the tip apex. Depending on the structure of the tip, typically from 30 nm to 200 nm of the PtIr tip apex is exposed.

DFT calculations

Spin-polarized DFT calculations are performed by using the Vienna ab initio simulation package (VASP) code^{36–39} and the core electrons are described by the projector augmented-wave method⁴⁰. Exchange correlation is treated in the generalized gradient approximation, as implemented by Perdew et al.⁴¹. The plane-wave basis is expanded to a cutoff of 600 eV and the Brillouin zone is sampled using Γ points only. Because of the relative importance of non-bonding molecule surface interactions, the van der Waals D3 functional is used⁴². The PBE + U method has been used for the exchange functional with U – J = 3 eV for the Fe ‘d’ states^{43–45}.

A <tpy-Fe-tpy> bridge composed of 79 atoms is placed on a three-layer Au(111) slab containing 252 atoms representing the Au(111) surface. The supercell has a vacuum space of 30 Å in the direction perpendicular to the surface plane and 20 Å between the neighbouring complexes. The geometry optimizations converge with a 2-meV threshold per formula unit for the total ground-state energies. To estimate the work function, we calculate the spherically averaged potential over the z direction of the cell (Extended Data Fig. 10). The vacuum level is located at 25 Å in the z direction. From the vacuum energy of 2.89 eV and the Fermi level of -1.51 eV, a work function of 4.40 eV is obtained.

The hybridization of Fe ‘d’ and N ‘p’ orbitals and the energetic positions of their unoccupied orbitals are also calculated using Gaussian 16 software package⁴⁶ to make a comparison with the DFT calculations using VASP code shown in Fig. 4e. Geometry optimization of <tpy-Fe-tpy>²⁺ is performed using DFT calculations implemented in Gaussian, and the B3LYP (refs. 47–49) density functional and def2TZVP (ref. 50) basis set are used. The density of states corresponding to Fe ‘d’ and N ‘p’ are extracted from the optimized geometry and their unoccupied levels are plotted (Extended Data Fig. 10). Comparison of the energy difference between each peak in experiment and theory are in reasonable agreement.

Data availability

All data are available in the main text, extended data and supplementary materials. The source data for the manuscript, for the extended data figures and Supplementary Figs. 13–16 are provided with the manuscript. All the theory data are deposited at <https://doi.org/10.19061/喬化-6-165>. Source data are provided with this paper.

31. Zhang, Z. et al. Intra- and intermolecular self-assembly of a 20-nm-wide supramolecular hexagonal grid. *Nat. Chem.* **12**, 468–474 (2020).
32. Newkome, G. et al. Nanoassembly of a fractal polymer: a molecular “Sierpinski hexagonal gasket”. *Science* **312**, 1782–1785 (2006).
33. Li, Y. et al. Anomalous Kondo resonance mediated by semiconducting graphene nanoribbons in a molecular heterostructure. *Nat. Commun.* **8**, 946 (2017).
34. Rose, V., Preissner, C. A., Hla, S.-W., Wang, K. & Rosenmann, D. Simultaneous topographic and elemental chemical and magnetic contrast in scanning tunneling microscopy. US patent 8,850,611 (2014).
35. Cummings, M. et al. Controlled modulation of hard and soft X-ray induced tunneling currents utilizing coaxial metal-insulator-metal probe tips. *J. Appl. Phys.* **121**, 015305 (2017).
36. Kresse, G. & Hafner, J. *Ab initio* molecular dynamics for liquid metals. *Phys. Rev. B* **47**, 558–561 (1993).
37. Kresse, G. & Hafner, J. *Ab initio* molecular-dynamics simulation of the liquid-metal–amorphous-semiconductor transition in germanium. *Phys. Rev. B* **49**, 14251–14269 (1994).
38. Kresse, G. & Furthmüller, J. Efficiency of ab-initio total energy calculations for metals and semiconductors using a plane-wave basis set. *Comput. Mater. Sci.* **6**, 15–50 (1996).
39. Kresse, G. & Furthmüller, J. Efficient iterative schemes for *ab initio* total-energy calculations using a plane-wave basis set. *Phys. Rev. B* **54**, 11169–11186 (1996).
40. Anisimov, V. I., Aryasetiawan, F. & Lichtenstein, A. I. First-principles calculations of the electronic structure and spectra of strongly correlated systems: the LDA+U method. *J. Phys. Condens. Matter* **9**, 767–808 (1997).
41. Perdew, J. P., Burke, K. & Ernzerhof, M. Generalized gradient approximation made simple. *Phys. Rev. Lett.* **77**, 3865–3868 (1996).
42. Grimme, S., Antony, J., Ehrlich, S. & Krieg, S. A consistent and accurate *ab initio* parametrization of density functional dispersion correction (DFT-D) for the 94 elements H–Pu. *J. Chem. Phys.* **132**, 154104 (2010).
43. Brena, B. & Herper, H. C. Influence of ligands on the electronic and magnetic properties of Fe porphyrin in gas phase and on Cu(001). *J. Appl. Phys.* **117**, 17B318 (2015).
44. Zhang, Z. & Satpathy, S. Electron-states, magnetism, and the Verwey transition in magnetite. *Phys. Rev. B* **44**, 13319–13331 (1991).
45. Dudarev, S. L., Botton, G. A., Savrasov, S. Y., Humphreys, C. J. & Sutton, A. P. Electron-energy-loss spectra and the structural stability of nickel oxide: an LSDA+U study. *Phys. Rev. B* **57**, 1505–1509 (1998).
46. Frisch, M. J. et al. Gaussian 16 (Gaussian, Inc., 2016).
47. Becke, A. D. Density-functional thermochemistry. III. The role of exact exchange. *J. Chem. Phys.* **98**, 5648–5652 (1993).
48. Lee, C., Yang, W. & Parr, R. G. Development of the Colle-Salvetti correlation-energy formula into a functional of the electron density. *Phys. Rev. B* **37**, 785–789 (1988).
49. Gill, P. M. W., Johnson, B. G., Pople, J. A. & Frisch, M. J. The performance of the Becke–Lee–Yang–Parr (B–LYP) density functional theory with various basis sets. *Chem. Phys. Lett.* **197**, 499–505 (1992).
50. Schäfer, A., Horn, H. & Ahlrichs, R. Fully optimized contracted Gaussian basis sets for atoms Li to Kr. *J. Chem. Phys.* **97**, 2571–2577 (1992).

Acknowledgements We acknowledge financial support from the U.S. Department of Energy, Office of Science, Office of Basic Energy Sciences, Materials Science and Engineering Division. Work performed at the Center for Nanoscale Materials and Advanced Photon Source, both U.S. Department of Energy Office of Science User Facilities, was supported by the U.S. Department of Energy, Office of Basic Energy Sciences, under Contract No. DE-AC02-06CH11357. We gratefully acknowledge the computing resources provided on Bebop, a high-performance computing cluster operated by the Laboratory Computing Resource Center at Argonne National Laboratory.

Author contributions S.-W.H. conceived and designed the experiments. T.M.A., S.Wieghold, N.S., S.-W.H., V.R. and S.P. performed the SX-STM experiments. D.J.T., K.Z.L., S.S., S.Wang and Y.Li prepared the samples and performed STM imaging. T.M.A., S.Wieghold, N.S. and S.-W.H analysed the SX-STM data. Y.Li and X.L. synthesized the Fe and Ru assemblies. E.M. designed the Tb complex, X.C. synthesized it and N.K. obtained its X-ray crystal structure. D.R. and Y.Li prepared the coaxial tips for SX-STM. T.R., N.K.D. and A.T.N. performed the calculations. All authors discussed the results and commented on the manuscript.

Competing interests The authors declare no competing interests.

Additional information

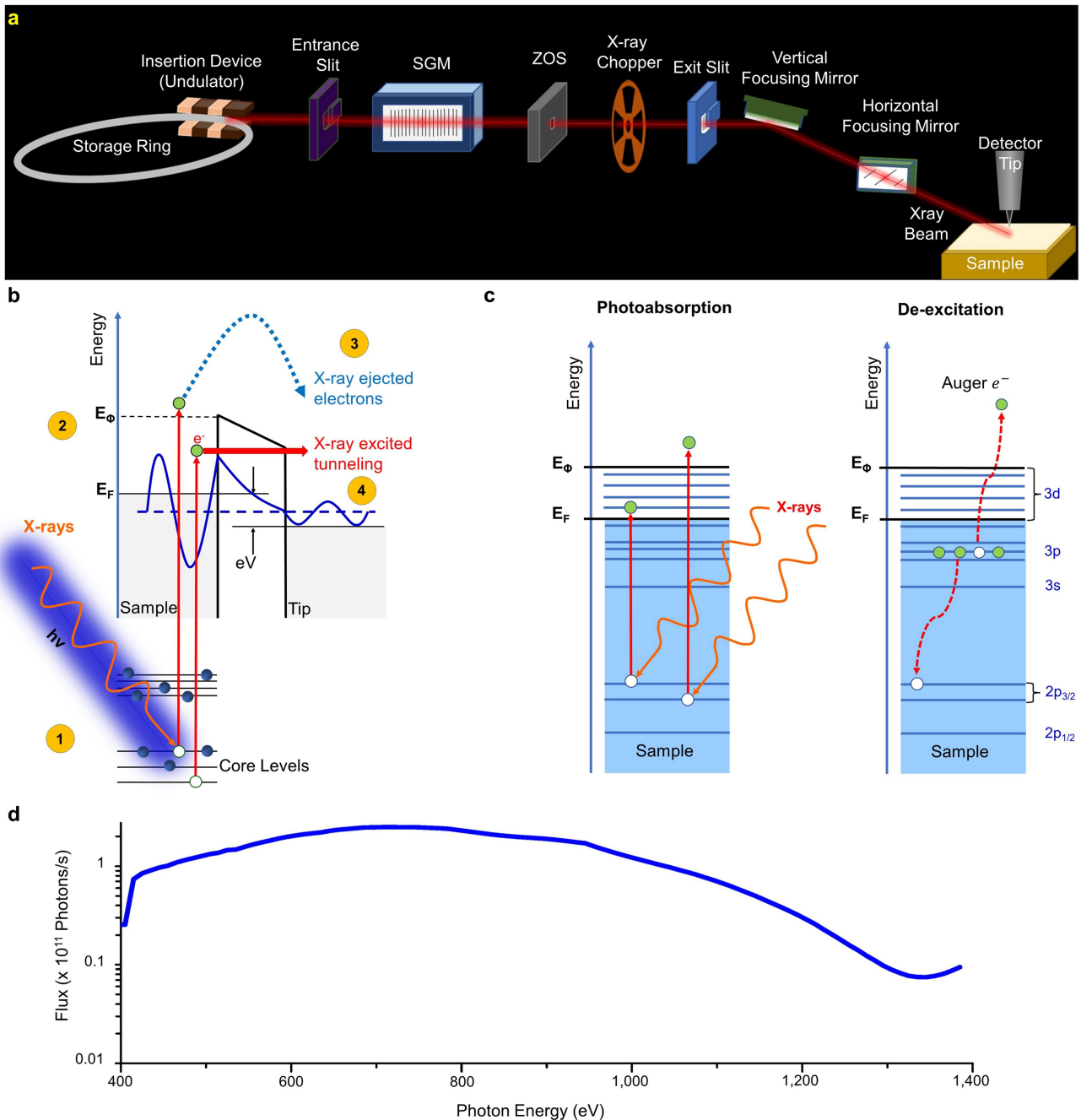
Supplementary information The online version contains supplementary material available at <https://doi.org/10.1038/s41586-023-06011-w>.

Correspondence and requests for materials should be addressed to Volker Rose or Saw-Wai Hla.

Peer review information *Nature* thanks the anonymous reviewers for their contribution to the peer review of this work.

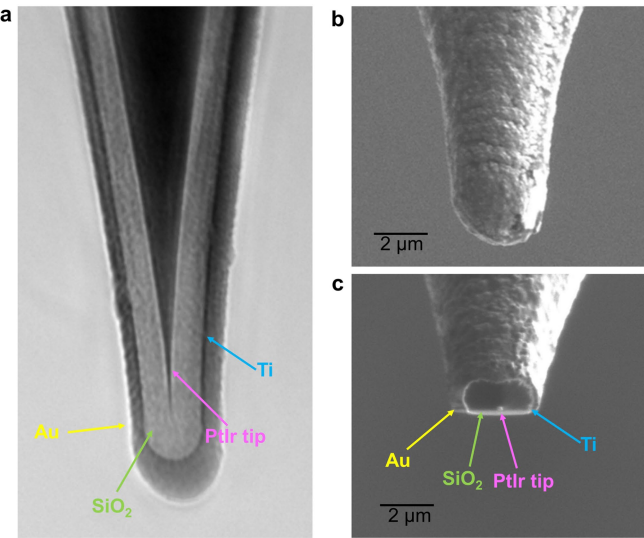
Reprints and permissions information is available at <http://www.nature.com/reprints>.

Article

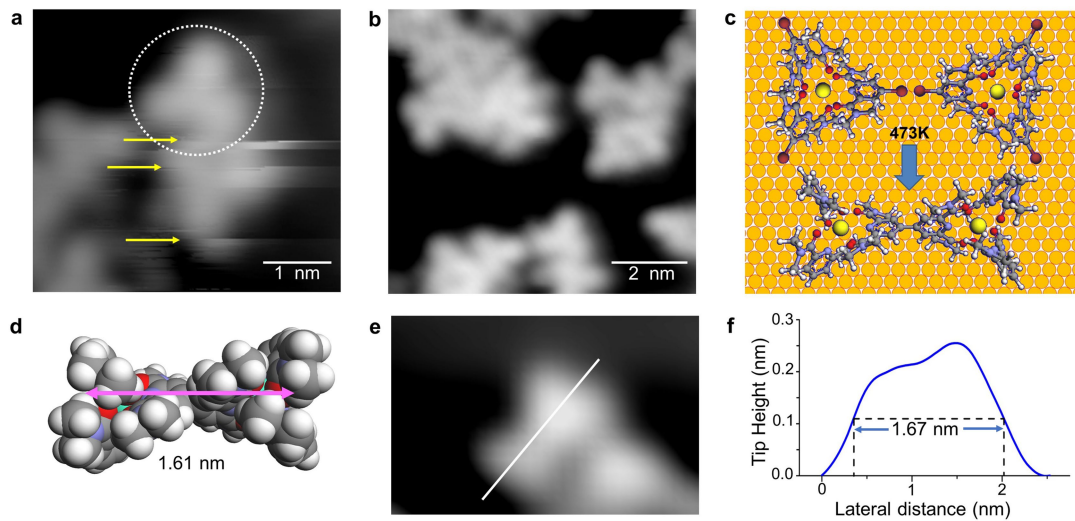


Extended Data Fig. 1 | XTIP beamline and SX-STM technique. **a**, Schematic presentation of XTIP. **b**, Mechanistic model of the SX-STM process. (1) Photoabsorption process. (2) X-ray-excited electrons and Auger electrons with energies between the Fermi level E_F and the work function Φ fill up unoccupied states of the sample, whereas those having energies exceeding the work function escape ('X-ray-ejected electrons'). (3) X-ray-ejected electrons captured by the tip produce a photocurrent. (4) The electrons that fill up states between E_F and Φ tunnel to the tip, generating an X-ray-excited

tunnelling current. Both the X-ray-ejected electron current and X-ray-excited tunnelling current are produced by the same initial photoabsorption process (1). **c**, Left, photoabsorption process excites core-level electrons either to unoccupied orbitals below the work function or above the vacuum level, depending on the energy of the photon. This process leaves a hole in a core level. Right, in the de-excitation process, an electron from a higher level fills up the hole. The excess energy can cause the release of Auger electrons. **d**, Measured photon flux of the XTIP beamline.

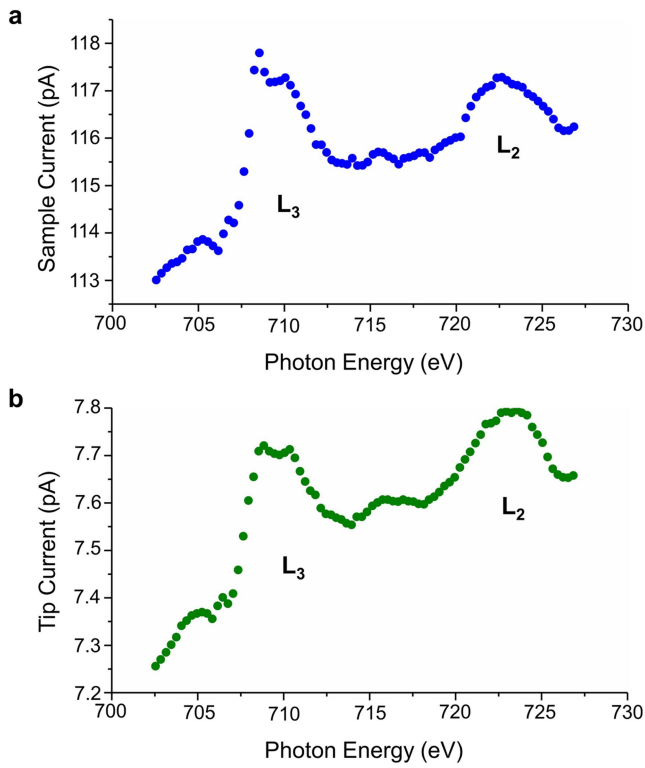


Extended Data Fig. 2 | Coaxial detector tip. **a**, Transmission X-ray microscopy image of a detector tip shows several materials composing the tip. Scanning electron microscopy image of a detector tip before (**b**) and after (**c**) incision. Here the PtIr conducting core is used to collect electrons, whereas the SiO_2 insulating layer prevents collection of ejected electrons from the sample by the side wall of the tip. The outer Au conducting layer is to protect from the charging effect^{34,35}.

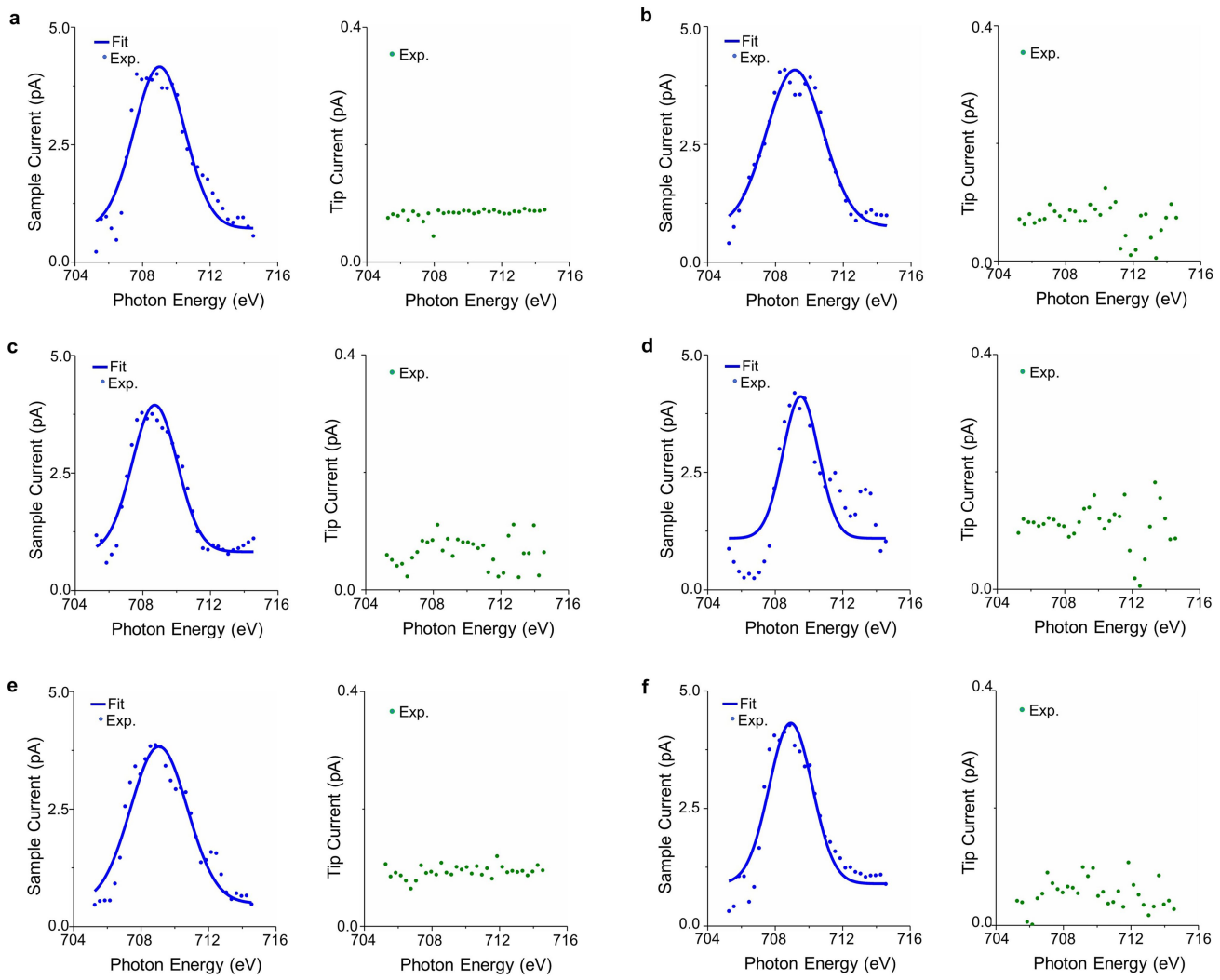


Extended Data Fig. 3 | Formation of dimer complexes through Ullmann coupling. **a**, STM images $\text{Tb}(\text{pcam-Br})_3$ on Au(111) acquired at 5 K substrate temperature. A single $\text{Tb}\text{-}(\text{pcam-Br})_3$ complex is indicated with a circle. $\text{Tb}(\text{pcam-Br})_3$ is mobile (indicated with arrows) during scanning with the STM tip even at 5 K. **b**, STM image of $\text{Tb}(\text{pcam-Br})_3$ clusters on Au(111). **c**, A model depicting debromination and covalent linking of two monomers (upper part).

Heating the sample to 473 K results in the formation of a dimer, $[\text{Tb}(\text{pcam})_3]_2$ (lower part). **d**, A model of $[\text{Tb}(\text{pcam})_3]_2$. The yellow balls in **c** and **d** are Tb ions. **e**, An STM image of a dimer. **f**, A profile measured along the white line shown in **e** gives the length of the dimer as roughly 1.67 nm, which agrees well with the expected length of about 1.61 nm shown in **d**. Image parameters for **a**, **b** and **e**: $I_t = 100 \text{ pA}$, $V_t = 0.5 \text{ V}$.

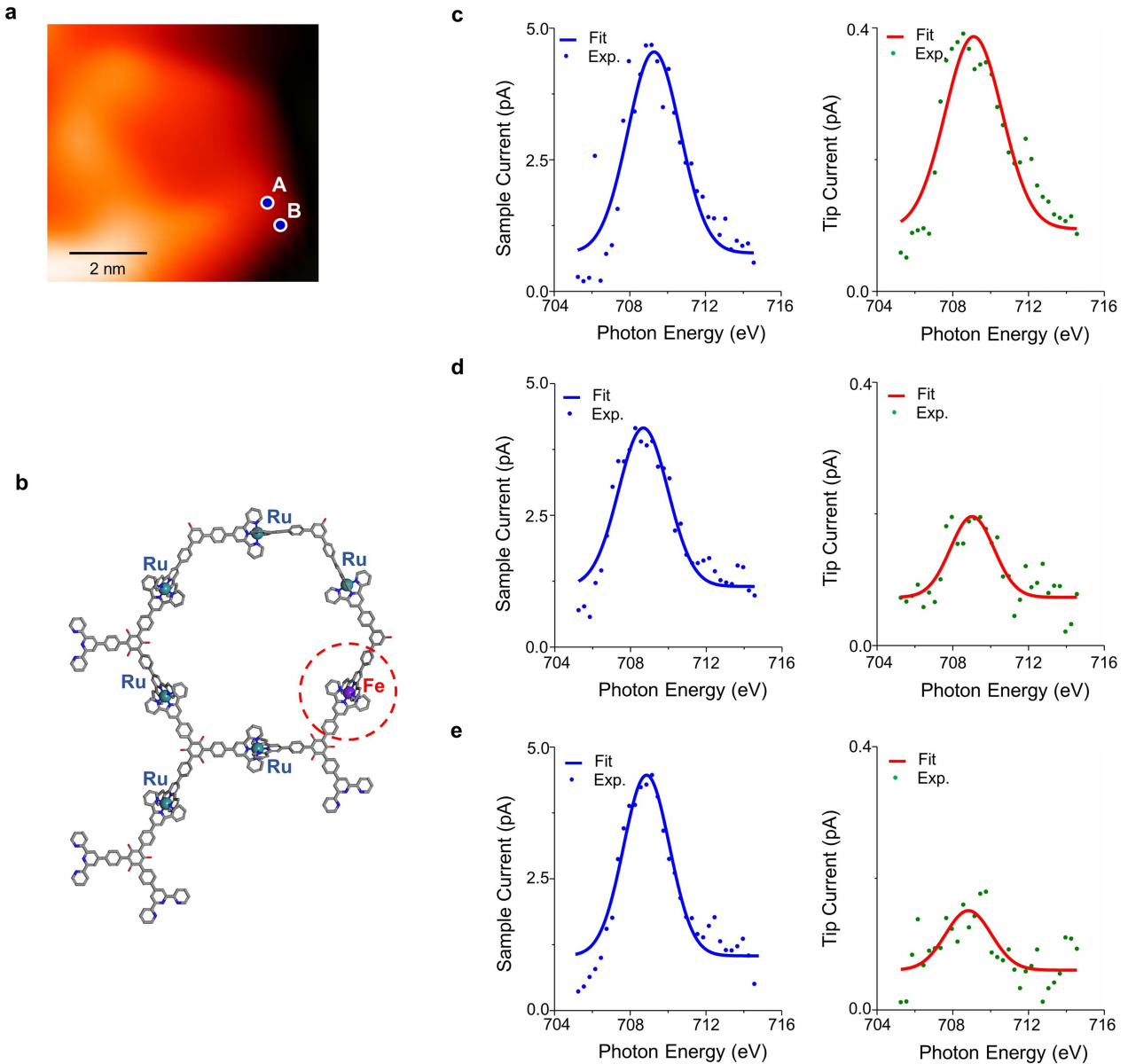


Extended Data Fig. 4 | Simultaneously measured X-ray-excited currents in the tunnelling regime before background subtraction. Sample channel (a) and tip channel (b). Background subtraction is performed by setting the photocurrent at 702.5 eV to zero and applying a linear slope correction.



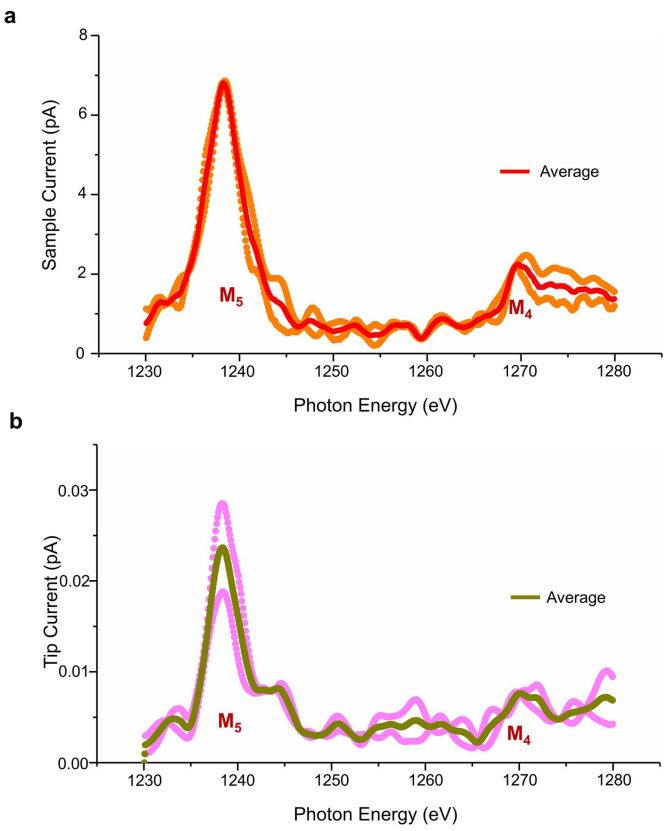
Extended Data Fig. 5 | STM-XAS on Ruions. The supramolecular ring (see Fig. 1a and Extended Data Fig. 6b) includes only one Fe ion and the rest of the tpy bridges are formed by Ru ions. **a–f**, Simultaneously measured STM-XAS spectra in the sample and tip channels focusing on the Fe L₃ edge region on the six <tpy-Ru-tpy> bridges. The tip channel in the tunnelling regime detects

atomically localized signal and, thus, it does not show any Fe L₃ edge signature when measured on the <tpy-Ru-tpy> bridges, because the Fe ions are not present there. However, the sample channel gives a strong Fe L₃ edge signal because it is produced by the entire X-ray-illuminated surface area in which many supramolecular rings, each having one Fe ion, are present.

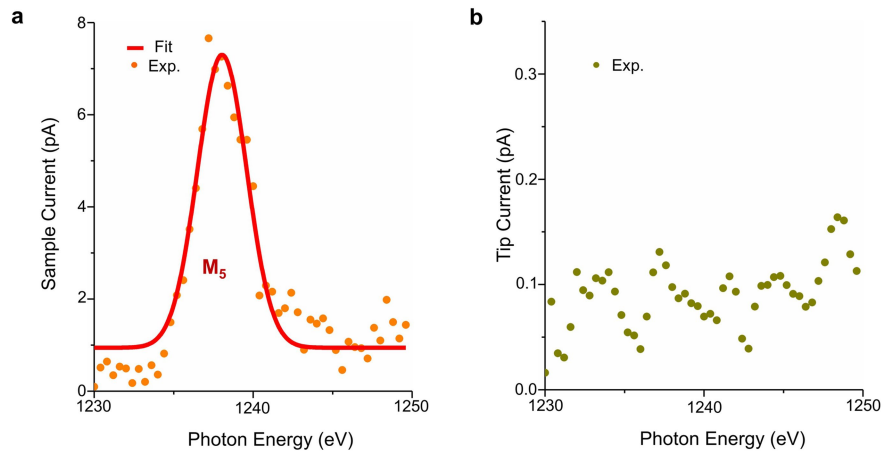


Extended Data Fig. 6 | STM-XAS on different locations of a <tpy-Fe-tpy> bridge. **a**, An STM image of a single supramolecular ring measured with the SX-STM setup. Image parameters: $I_t = 100$ pA, $V_t = -1.0$ V. **b**, Atomic positions of Fe and Ru ions in **a**. **c–e**, Simultaneously measured STM-XAS spectra in sample and tip channels in the tunnelling regime focusing on the L₃ absorption edge of

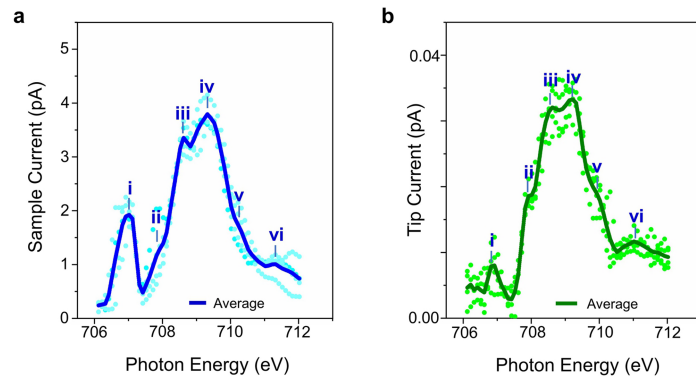
Fe. Cogent L₃ edge signals of Fe ion are observed in both the sample and tip channels in **c** measured at the centre of the <tpy-Fe-tpy> bridge in which the Fe ion is located (position A in **a**). Weak Fe edge signals are observed when measured on the <tpy-Fe-tpy> bridge but the tip is not positioned on top of the Fe ion, such as in position B (**d** and **e**).



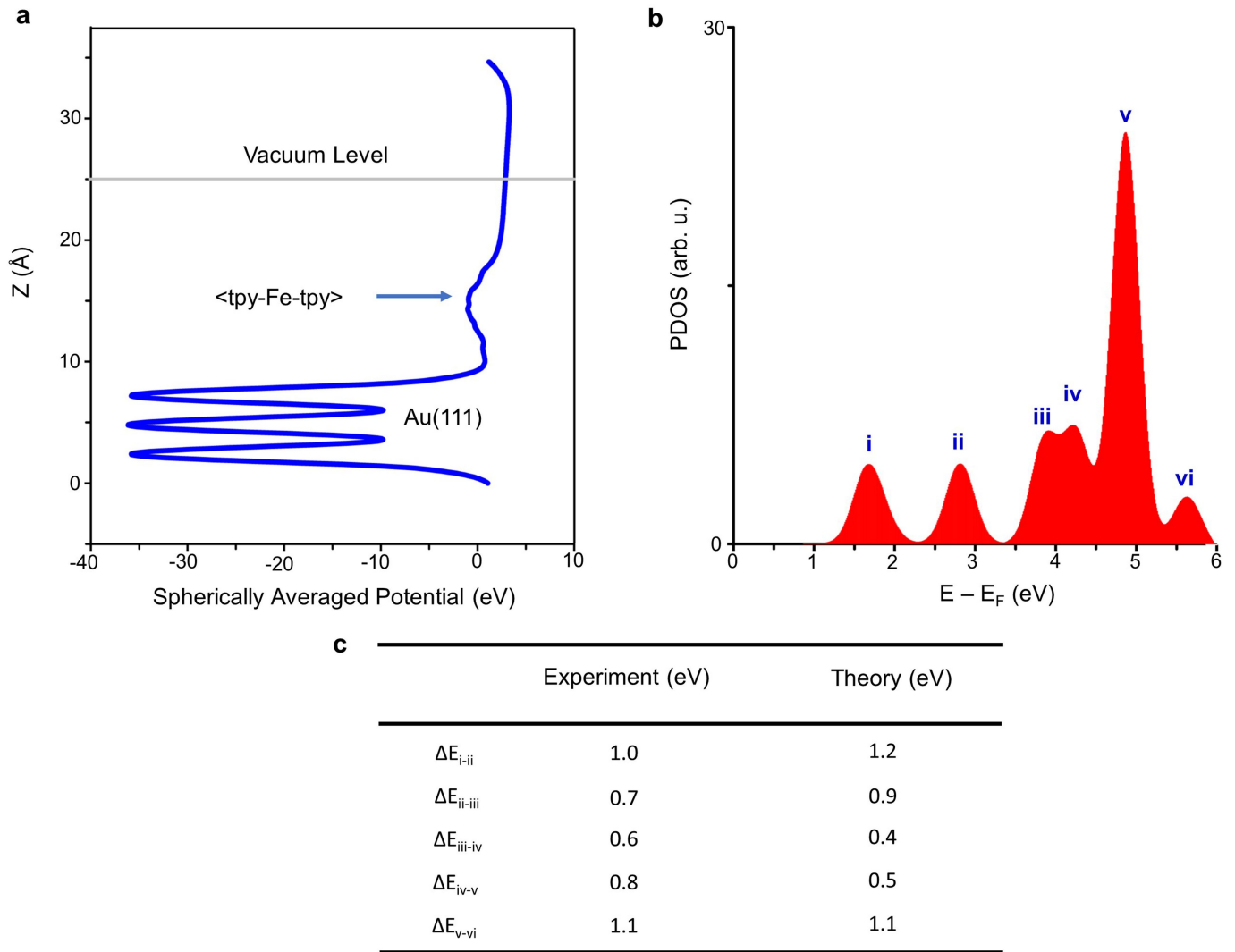
Extended Data Fig. 7 | STM-XAS spectra of Tb M_{4,5} absorption edges in the far-field regime. At the sample channel (**a**) and at the tip channel (**b**).



Extended Data Fig. 8 | STM-XAS signals in the tunnelling regime when the tip is not on top of the Tb ion. The sample channel (**a**) and the tip channel (**b**).



Extended Data Fig. 9 | STM-NEXAFS spectra of Fe ion in the far field. The sample channel (a) and the tip channel (b). The satellite peaks are labelled as i, ii, iii, iv, v and vi.



Extended Data Fig. 10 | Theory calculations. **a**, Spherically averaged potential of the $\langle \text{tpy-Fe-tpy} \rangle$ bridge on Au(111). The vacuum level is indicated. PDOS of combined Fe 'd' and N 'p' orbitals calculated by B3LYP/def2TZVP-based

theory (**b**) and energy differences between the peaks in **b** with the experimentally measured data (**c**).